The Astrophysical Journal, 757:113 (8pp), 2012 October 1 doi:10.1088/0004-637X/757/2/113

SOFIA/FORCAST AND *SPITZER*/IRAC IMAGING OF THE ULTRACOMPACT H II REGION W3(OH) AND ASSOCIATED PROTOSTARS IN W3

Lea Hirsch[1], Joseph D. Adams[1], Terry L. Herter[1], Joseph L. Hora[2], James M. De Buizer[3], S. Thomas Megeath[4], George E. Gull[1], Charles P. Henderson[1], Luke D. Keller[5], Justin Schoenwald[1], and William Vacca[3]
[1] Department of Astronomy, Cornell University, 105 Space Sciences Building, Ithaca, NY 14853, USA
[2] Harvard-Smithsonian Center for Astrophysics, 60 Garden Street, MS 65, Cambridge, MA 02138-1516, USA
[3] SOFIA-University Space Research Association, NASA Ames Reseach Center, Mail Stop N211-3, Moffett Field, CA 94035, USA
[4] Department of Physics and Astronomy, University of Toledo, Mailstop 111, 2801 West Bancroft Street, Toledo, OH 43606, USA
[5] Ithaca College, Physics Department, 264 Center for Natural Sciences, Ithaca, NY 14850, USA
Received 2012 June 18; accepted 2012 August 7; published 2012 September 10

ABSTRACT

We present infrared observations of the ultracompact H II region W3(OH) made by the FORCAST instrument aboard the *Stratospheric Observatory for Infrared Astronomy* (*SOFIA*) and by the *Spitzer*/Infrared Array Camera. We contribute new wavelength data to the spectral energy distribution (SED), which constrains the optical depth, grain size distribution, and temperature gradient of the dusty shell surrounding the H II region. We model the dust component as a spherical shell containing an inner cavity with radius ∼600 AU, irradiated by a central star of type O9 and temperature ∼31,000 K. The total luminosity of this system is $7.1 \times 10^4\ L_\odot$. An observed excess of 2.2–4.5 μm emission in the SED can be explained by our viewing a cavity opening or clumpiness in the shell structure whereby radiation from the warm interior of the shell can escape. We claim to detect the nearby water maser source W3 (H_2O) at 31.4 and 37.1 μm using beam deconvolution of the FORCAST images. We constrain the flux densities of this object at 19.7–37.1 μm. Additionally, we present in situ observations of four young stellar and protostellar objects in the *SOFIA* field, presumably associated with the W3 molecular cloud. Results from the model SED fitting tool of Robitaille et al. suggest that two objects (2MASS J02270352+6152357 and 2MASS J02270824+6152281) are intermediate-luminosity (∼236–432 $L_\odot$) protostars; one object (2MASS J02270887+6152344) is either a high-mass protostar with luminosity $3 \times 10^3\ L_\odot$ or a less massive young star with a substantial circumstellar disk but depleted envelope; and the other (2MASS J02270743+6152281) is an intermediate-luminosity (∼768 $L_\odot$) protostar nearing the end of its envelope accretion phase or a young star surrounded by a circumstellar disk with no appreciable circumstellar envelope.

Key words: circumstellar matter – H II regions – infrared: stars – radiative transfer – stars: formation

1. INTRODUCTION

Ultracompact H II regions (UCHs) can be found throughout the Galaxy surrounding newly formed massive stars just completing the accretion stage and entering their main-sequence lifetimes. UCHs are small (<0.4 pc), hot (>100 K), and massive ($>10^3\ M_\odot$), and emit 10^4–$10^6\ L_\odot$ (Churchwell 2002). These regions of ionized gas are surrounded by molecular and dust clouds, out to as far as 10 times the radius of the UCHs themselves (Conti et al. 2008). This causes attenuation of much of the emitted luminosity, as it is absorbed and reradiated in the infrared.

W3(OH) is one of the largest and best-studied UCH II regions known in the Galaxy. It is at a distance of approximately 2.04 kpc in the Perseus arm (HaChisuka et al. 2006). Like most UCH II regions, it is surrounded by its natal dust and molecular gas envelope as well as a larger giant molecular cloud encompassing W3(OH) and W3(H_2O), W3 Main, and AFGL 333; these are all regions of potentially triggered star formation, based on their positions on the dense outskirts of a much less dense cavity in the W3 GMC (Ruch et al. 2007; Moore et al. 2007). A further review of star formation in the W3 GMC is presented by Megeath et al. (2008).

Line emission from the molecular gas surrounding W3(OH) has been mapped at submillimeter and radio wavelengths in the transitions of OH and H_2O (Mader et al. 1978), HCN (Turner & Welch 1984), NH_3 (Wilson et al. 1978; Zeng et al. 1984; Tieftrunk et al. 1998), CH_3OH (Menten et al. 1992), $C^{18}O$ (Wink et al. 1994), and $C^{17}O$ (Wyrowski et al. 1997). This molecular emission is found out to a 1′ diameter region. These studies have particularly focused on further characterizing the molecular gas and the OH and methanol masers within and around W3(OH), as well as the hot core/water maser region W3(H_2O) approximately 6″ to the east. In continuum emission, however, the dust cocoon surrounding the UCH II region comes into primary focus.

The dust component to the UCH II W3(OH) was detected by Wynn-Williams et al. (1972) at ∼1–20 μm; the dust component is optically thick in the near- and mid-infrared. Chini et al. (1986) studied the cold dust at wavelengths of 350 μm and 1.3 mm. Using a spherically symmetric radiative transfer model, they concluded that the inner cavity ($\lesssim 2 \times 10^{17}$ cm) of the UCH II region is depleted of dust, rather than having dust density that increases approaching the central star. A large amount of visual extinction ($A_v \sim 67$) in a thick outer shell was required to explain the decline in emission at $\lambda \lesssim 5\ \mu$m. Utilizing airborne data, Campbell et al. (1989) showed that the dust cocoon is optically thick in the far-infrared and developed a more detailed model containing an H II region and a cavity. Surrounding the cavity is a dusty region with a free-fall density distribution and a temperature gradient through the dust cloud. More recently, Stecklum et al. (2002) presented high spatial resolution, ground-based 10 and 20 μm images of W3(OH). From these data, the model for the dust shell was further developed and contained a Gaussian density distribution with an inner cavity of radius 2270 AU and stellar luminosity of $8 \times 10^4 L_\odot$.

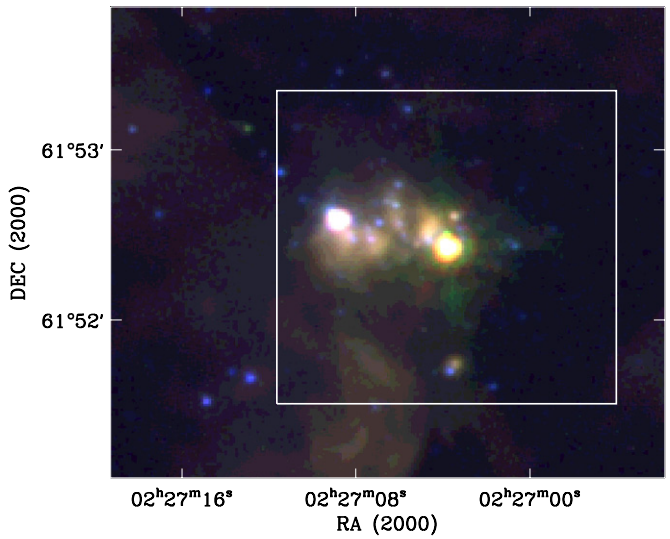

Figure 1. False-color IRAC image of the W3(OH) region at 3.6 μm (blue), 5.8 μm (green), and 8.0 μm (red). The box indicates the region of the *SOFIA* field that is shown in Figure 2.

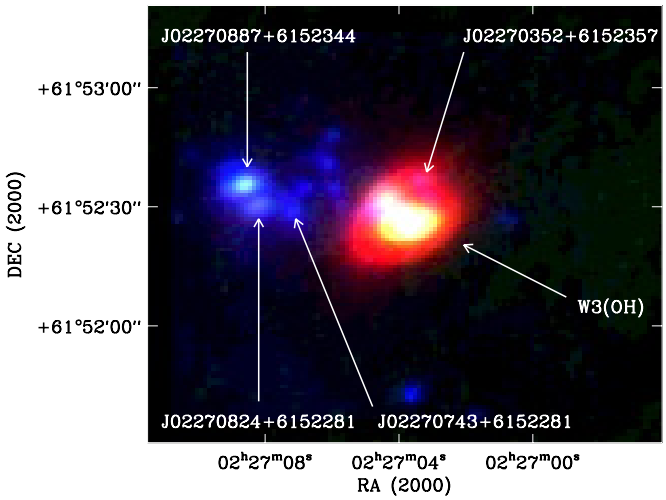

Figure 2. False-color image of the W3(OH) region at 3.6 μm (blue, IRAC), 19.7 μm (green, FORCAST), and 37.1 μm (red, FORCAST). The image at 3.6 μm was convolved with a Gaussian kernel to match the spatial resolution of FORCAST at 37.1 μm. The positions of W3(OH) and the four point sources that were detected by *SOFIA*/FORCAST are indicated.

In this work, we present new, high spatial resolution observations of the W3(OH) region in the wavelength range ~3.6–40 μm obtained with the FORCAST instrument (Herter et al. 2012) on the *Stratospheric Observatory for Infrared Astronomy* (*SOFIA*; Young et al. 2012) and with the Infrared Array Camera (IRAC; Fazio et al. 2004) on the *Spitzer Space Telescope* (Werner et al. 2004). These wavelengths are critical for determining the spectral energy distribution (SED) of the W3(OH) dust cocoon and thus for making a measurement of its total luminosity. We combine our data with Two Micron All Sky Survey (2MASS; Skrutskie et al. 2006) fluxes and other data published in the literature to construct SEDs for the W3(OH) dust component. We model the dust component as a dusty shell around the H II region and compute the emergent flux using radiative transfer code. In addition, we present in situ observations of four stellar and protostellar objects in the *SOFIA*/FORCAST field. We fit the SEDs of these objects to those of high- and intermediate-mass protostars containing dusty circumstellar envelopes and circumstellar disks. We discuss the physical properties of all these objects.

2. OBSERVATIONS

2.1. *SOFIA*/FORCAST Observations

Observations were conducted on 2010 December 8 aboard the *SOFIA*, using the Cornell-built FORCAST (Adams et al. 2010). FORCAST uses an Si:As BIB detector array at wavelengths $\lambda \leqslant 26$ μm and an Si:Sb BIB array at $\lambda \geqslant 26$ μm. The detector has a 0.″7638 pixel scale (rectified) over a total field of view of 3.′4 × 3.′2. Four filters were utilized for these observations, with central wavelengths (and bandpasses) at 19.7 (5.5), 24.2 (2.9), 31.4 (5.7), and 37.1 (3.3) μm. The dichroic beamsplitter was used to obtain the wavelength pairs 19.7/37.1 and 24.2/31.4 μm. Asymmetrical chopping with respect to the optical axis was applied in order to avoid telescope coma in the on-source beam. The chop throw was 5′ and was designed to chop off nearby nebulosity. A five-point dither pattern in C2NC2 mode (Herter et al. 2012) was implemented to remove bad pixels during post-processing. Integration times were 30 s at every dither position which yielded a total of 150 s in each filter configuration. The data were pipeline processed with the reduction algorithms described in Herter et al. (2012). A global solution to the calibration from the *SOFIA* Early Science phase was applied to the images (Herter et al. 2012). We discuss flux extraction of sources in Section 3. Finally, we applied color corrections to the extracted fluxes as computed by an instrument model with model atmosphere (Herter et al. 2012).

2.2. *Spitzer*/IRAC Observations

We used data obtained with IRAC on *Spitzer*. The data were taken from observations that were obtained in high dynamic range mode, whereby two images are taken in succession at 0.4 s and 10.4 s integration times. The brightest objects in the field, including W3(OH) were saturated in the longer frames, so we used the 0.4 s exposure time frames to construct the mosaic that was used for the bright source photometry. The following AORIDs were used: 5050624, 19305728, 20590592, 38744064, 38757632, 38763776, 38769408, 38770944, 38790656, and 38801408. We utilized the Basic Calibrated Data (BCD) version S18.5 products from the Spitzer Science Center (SSC) standard data pipeline. For the 3.6 and 4.5 μm bands, data from the cryogenic and warm mission were combined. For the 5.8 and 8.0 μm BCDs, bright source artifacts such as "banding" (Hora et al. 2004) were removed using the IMCLEAN image processing routines.[6] The images were mosaiced with IRACproc (Schuster et al. 2006) which uses a version of the mopex mosaicing software (Makovoz & Khan 2005) developed at the SSC. The final mosaic was made with a pixel scale of 0.″863 pixel^{-1}.

3. RESULTS

3.1. Imagery and *SOFIA*/FORCAST Detections

Reduced, multi-wavelength IRAC and FORCAST images are shown in Figures 1 and 2. The measured image quality in the FORCAST images was consistent with the overall image quality achieved by *SOFIA* during the Early Science period (Herter et al. 2012). W3(OH) is spatially resolved in the FORCAST

[6] http://irsa.ipac.caltech.edu/data/SPITZER/docs/dataanalysistools/tools/contributed/irac/imclean/

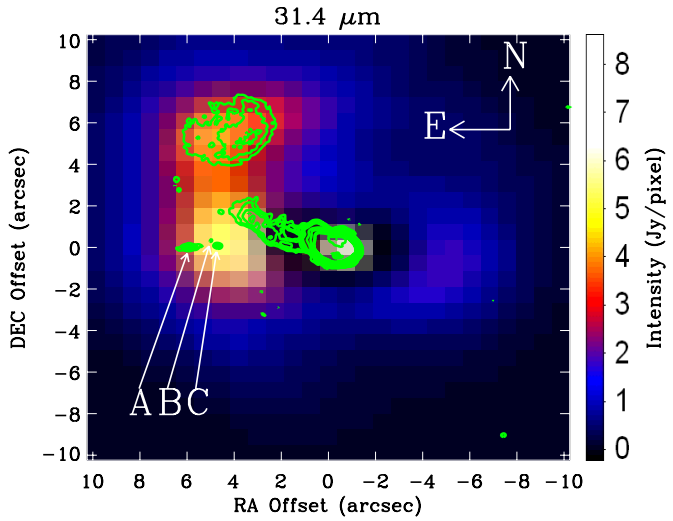

Figure 3. Deconvolved *SOFIA*/FORCAST image of W3(OH) at 31.4 μm, scaled linearly in flux. The image is centered on the coordinates R.A. = $02^{h}27^{m}03\overset{s}{.}87$ and decl. = +61°52′24.″6 (J2000). The core of W3(OH) has been subtracted using a two-dimensional Gaussian fit to its radial brightness profile. The locations of sources A, B, and C in W3(H_2O) from Wyrowski et al. (1999) are shown. The green contours represent 8.4 GHz VLA observations from Wilner et al. (1999). The contours levels are 0.00004, 0.0001, 0.00018, 0.0003, 0.0005, 0.001, 0.005, 0.01, 0.015, 0.016, 0.02, 0.022, and 0.03 Jy beam^{-1}. An assumption is that the peak of the 8.4 GHz contours coincides with the peak of the 19.7–37.1 μm emission. Also seen is the H II region to the northeast of the peak of W3(OH).

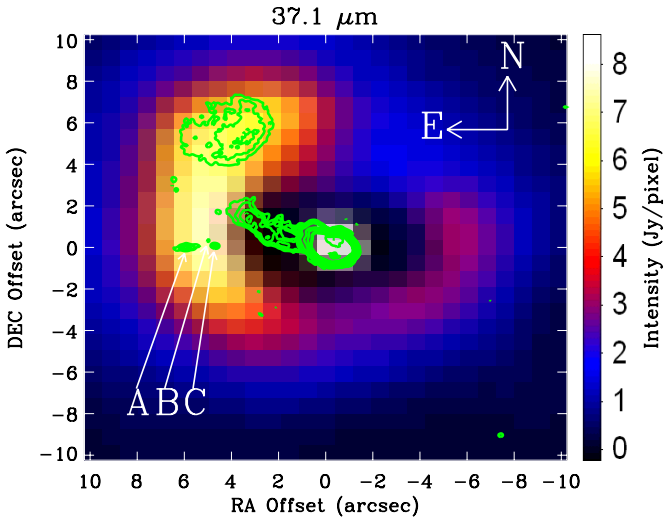

Figure 4. Same as Figure 3 for 37.1 μm.

images. Within W3(OH), the dual peaks in flux correspond to a bright cometary southwestern H II region and a dimmer, more eliptically shaped northeastern H II region (Stecklum et al. 2002).

We detect four mid-infrared point sources in the *SOFIA* field. These sources are designated in the 2MASS catalog as J02270352+6152357, J02270743+6152281, J02270824+6152281, and J02270887+6152344. There are also 2 μm counterparts to these sources in the K'-band image of Tieftrunk et al. (1998). However, there is a set of rich clusters of low-mass stars in this region, so confusion with neighboring sources precludes our making an accurate measurement of their 2 μm fluxes. In Figure 2, we label the sources with their corresponding designations. All four sources were detected by *SOFIA*/FORCAST at 19.7, 24.2, and 31.5 μm; J02270352+6152357, J02270824+6152281, and J02270887+6152344 were also detected at 37.1 μm. In addition, all four sources were detected in the *Spitzer* images at wavelengths of 3.6, 4.5, 5.8, and 8.0 μm; however, the 8.0 μm detection for J02270743+6152281 suffers from contamination by relatively bright nebulosity extending from below the source. The fluxes for J02270743+6152281, J02270824+6152281, and J02270887+6152344 were extracted from FORCAST images by fitting Gaussian functions to flux line profiles and from *Spitzer* images by aperture photometry. The corresponding flux densities are given in Table 1. Flux extraction for J02270352+6152357 is discussed in Section 3.2.

3.2. Deconvolved FORCAST Images

We performed beam deconvolution on each of the FORCAST images in order to search for the hot core W3(H_2O) and to measure the size of W3(OH). The images were deconvolved using the maximum likelihood method (Richardson 1972; Lucy 1974). Like all deconvolution methods, knowledge of the point-spread function (PSF) of an unresolved source is needed at each wavelength. The delivered PSF can change due to different wind loads on the secondary mirror and differences in the telescope flexure as a function of telescope position. To mitigate these effects on ground-based telescopes, high signal-to-noise (S/N) observations of mid-infrared bright stars are usually taken immediately before and/or after each science target observation and as close to the science target as possible (<1° away) so as to get the best PSF calibration for use in the deconvolution procedure. However, in our case, finding a PSF star that is bright enough at wavelengths out to 40 μm that fulfils these requirements is nearly impossible and thus was not attempted. Standard star images taken throughout our flight similarly did not have sufficient S/N for use as a PSF calibrator at the longer wavelengths. Therefore, we used these standard stars observations to determine an average FWHM for each wavelength for the flight. Then artificially generated PSFs (using an Airy pattern calculated from the wavelength, telescope diameter, and central obscuration diameter) were constructed and convolved with a Gaussian to achieve PSFs with FWHMs that equaled the measured average FWHMs of the standard stars. These idealized PSFs were then used in the deconvolution procedure. These deconvolved images compare favorably to simple unsharp masking of the original images, and hence all of the substructures revealed in the deconvolved images are believed to be real with high confidence. Final image resolutions are about a factor of two better than the natural resolutions for each image.

We claim to detect unresolved emission from the hot core W3(H_2O) at 31.4 and 37.1 μm. Figures 3 and 4 show the region near W3(H_2O) in the deconvolved images at 31.4 and 37.1 μm, respectively. In each case, the central core of W3(OH) has been fit to a two-dimensional Gaussian function and subtracted from the respective image. Figures 3 and 4 also contain 8.4 GHz Very Large Array (VLA) observations from (Wilner et al. 1999). The radio continuum image shows a cometary component extending in the northeast direction from the peak of W3(OH). The radio image also shows emission from the northeast H II region (Stecklum et al. 2002) above the cometary component. In the 8.4 GHz continuum, the W3(H_2O) clumps A, B, and C (Wyrowski et al. 1999) are resolved. Figures 3 and 4 show residual emission at 31.4 and 37.1 μm in the vicinity of W3(H_2O). Moreover, the position of this residual emission shifts

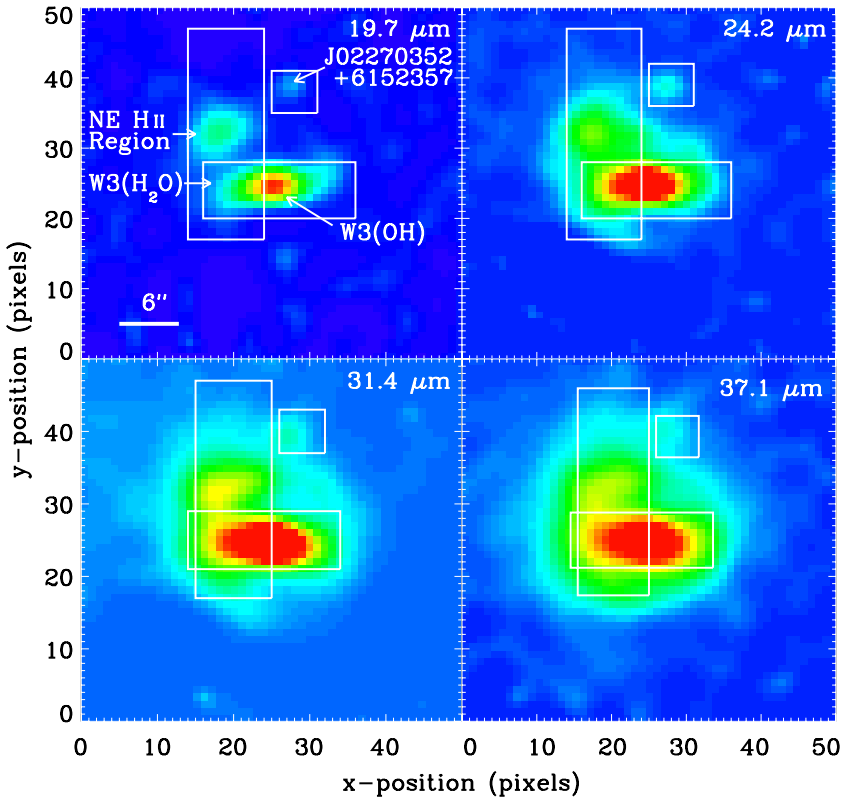

Figure 5. *SOFIA*/FORCAST deconvolved images at 19.7, 24.2, 31.4, and 37.1 μm, scaled logarithmically in flux with rainbow color intensity mapping. The locations of W3(OH), W3(H_2O), the northeastern H II region (Stecklum et al. 2002), and the point source 2MASS J02270352+6152357 are indicated in the upper left panel. The boxed regions were the regions selected for flux extraction; one-dimensional integrations were performed over the short dimensions of the boxes and the resulting line profiles are shown in Figure 6.

Table 1
Positions and Flux Densities in Janskies for W3(OH), W3(H_2O), and Four Mid-IR Sources in the SOFIA Field

	J02270352+6152357	W3(OH)	Northeastern H II	W3(H_2O)	J02270743+6152281	J02270824+6152281	J02270887+6152344
R.A. (2000)	02 27 03.52	02 27 03.83			02:27:07.43	02:27:08.24	02:27:08.87
decl. (2000)	+61 52 35.7	+61 52 24.8			+61:52:28.1	+61:52:28.1	+61:52:34.4
$F_{2.16}$	...	$1.76 \times 10^{-3} \pm 2.36 \times 10^{-4}$	...	...	...	...	...
$F_{3.6}$	0.0262 ± 0.00013	0.619 ± 0.00027	...	...	0.0691 ± 0.026	0.120 ± 0.00018	1.96 ± 0.00027
$F_{4.5}$	0.0470 ± 0.000088	3.74 ± 0.00018	...	...	0.0759 ± 0.026	0.137 ± 0.00012	2.97 ± 0.00018
$F_{5.8}$	0.237 ± 0.00054	11.8 ± 0.0011	...	...	0.364 ± 0.15	0.613 ± 0.00072	4.76 ± 0.0011
$F_{8.0}$	0.584 ± 0.00030	24.9 ± 0.00060	...	...	1.08 ± 0.41	1.66 ± 0.00040	9.43 ± 0.00060
$F_{19.7}$	1.53 ± 0.31	144 ± 37	19.7 ± 3.9	9.41 ± 1.9	1.28 ± 0.26	4.86 ± 0.97	12.8 ± 2.6
$F_{24.2}$	4.68 ± 0.94	683 ± 148	79.1 ± 16	76.7 ± 15	2.70 ± 0.54	10.5 ± 2.1	23.1 ± 4.6
$F_{31.4}$	10.6 ± 2.1	1626 ± 332	170 ± 34	147 ± 29	3.32 ± 0.66	15.0 ± 3.0	29.0 ± 5.8
$F_{37.1}$	13.0 ± 2.6	3232 ± 646	223 ± 45	225 ± 45	...	16.4 ± 3.3	40.9 ± 8.2

in wavelength from close to W3(H_2O) C at 31.4 μm toward W3(H_2O) A at 37.1 μm.

Flux extraction for W3(OH), W3(H_2O), the northeast H II region, and 2MASS J02270352+6152357 was performed using the deconvolved images. The resolved diameter of W3(OH) in the deconvolved images (Figure 5) is approximately 40 pixels, corresponding to ~63,000 AU. We used a 15 pixel aperture radius to extract the flux density at 19.7 μm and 20 pixel aperture radii to extract the flux densities at 24.2, 31.4, and 37.1 μm; we then subtracted the flux densities measured for the northeastern H II region and 2MASS J02270352+6152357 (discussed next). The resulting integrated flux densities for W3(OH) are listed in Table 1.

Figure 5 shows boxed regions where the flux profiles for W3(OH) and W3(H_2O) were extracted (integrated vertically) and fit to Gaussian functions (Figure 6). Each of the profiles shows a secondary peak coincident with the location of W3(H_2O). The area under the profile fit to W3(H_2O) yields its flux. The extracted flux densities for W3(H_2O) are also listed in Table 1. We discuss our detection of this source further in Section 4.2. The flux densities for W3(OH) measured in this fashion agree to within ~10% of the flux density measured from large aperture photometry, which is listed in Table 1.

Figure 5 also shows the regions selected for line profiles of the northeastern H II region (integrated horizontally) and 2MASS J02270352+6152357 (integrated vertically). The latter source is flagged in the 2MASS catalog as confused with neighboring objects; thus we do not consider its 2 μm flux. The line profiles for these one-dimensional integrations are shown in Figure 6 and their flux densities, determined by Gaussian line fits, are listed in Table 1.

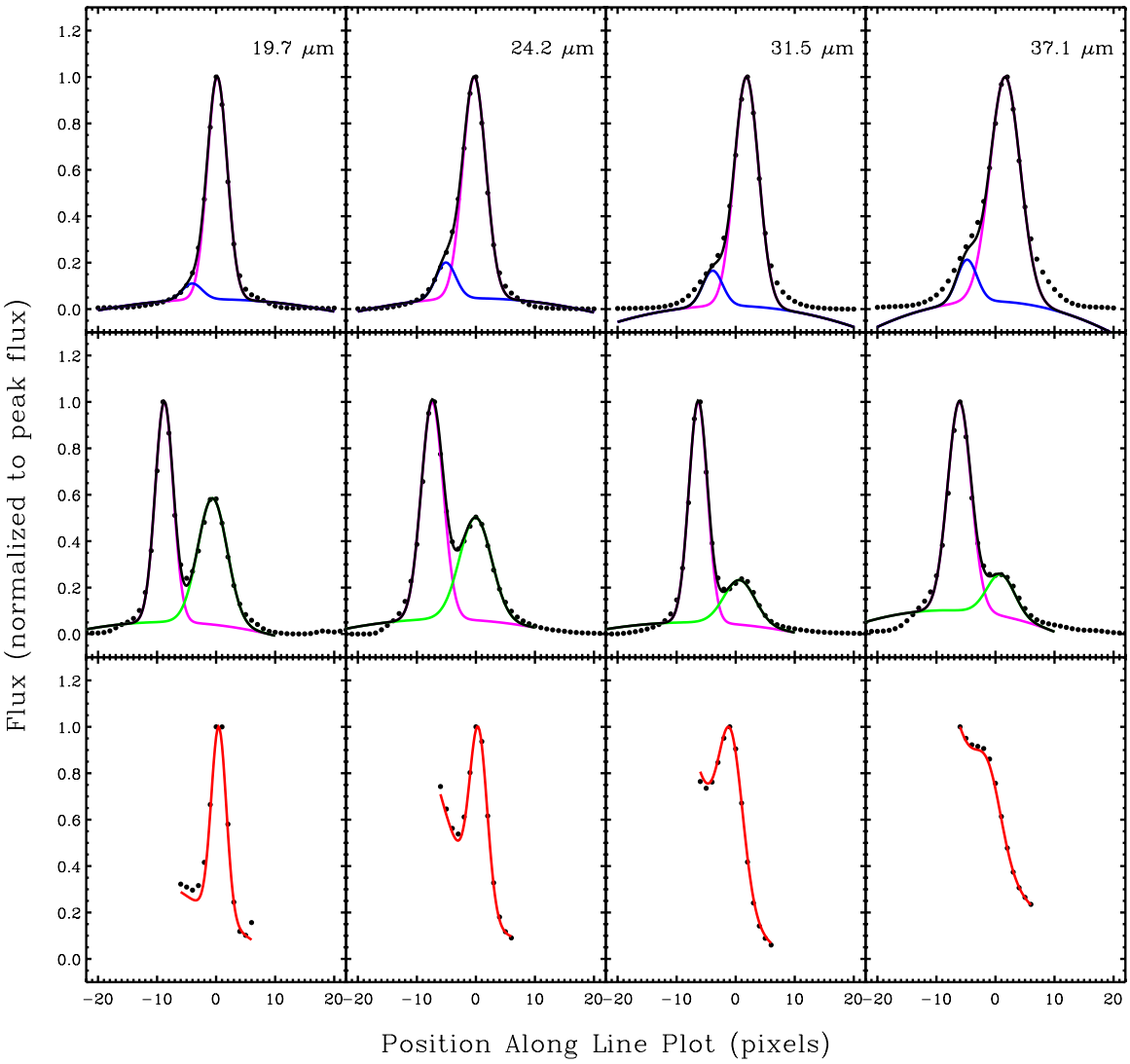

Figure 6. One-dimensional integrated and normalized line profiles (points) and best Gaussian fits for W3(OH) (magenta line), W3(H_2O) (blue line), the northeastern H II region (green line), and the point-source 2MASS J02270352+6152357 (red line). The one-dimensional integrations were performed along the short directions of the boxes in Figure 5. The black lines represent the sum of the fits. The extracted flux densities for all sources are given in Table 1.

4. DISCUSSION

4.1. W3 (OH)

In Figure 7, we show the SED for W3 (OH) with additional data taken from the literature: 2MASS (2.2 μm), Stecklum et al. (2002) (8.8, 12.7, and 17.8 μm), *Midcourse Space Experiment* (21 μm, Egan et al. 1999), *IRAS* (60 and 100 μm), and Chini et al. (1986) (1.3 mm). The *IRAS* flux densities were taken as upper limits due to contamination from nearby sources.

We model the dust component as an optically thick, dusty shell around the H II region, irradiated at the inner boundary by the central star with surface temperature 3.11×10^4 K. The emergent SED of the model was computed using the DUSTY radiative transfer code.[7] The density distribution of this model ($\rho \propto r^{-p}$; $p = 1.5$) is based on a free-fall density profile (e.g., Hartmann 2009). We chose the composition of the dust to be 53% silicates and 47% graphite grains (Draine & Lee 1984). We consider a grain size distribution $n(a) \propto a^{-q}$, whereby $q = 3.5$ (Mathis et al. 1977; hereafter MRN), and with a minimum grain size of 0.001 μm and a maximum grain size of 0.25 μm (MRN; Sellgren 1984). We set the temperature of the inner edge of the shell at 400 K for this model. This is substantially cooler than the dust sublimation temperature (~1500 K), indicating the presence of a large cavity depleted of dust and consistent with previous work (Chini et al. 1986; Stecklum et al. 2002). The total luminosity of this model is $\sim 7.1 \times 10^4\ L_\odot$. The SED of this model is shown in Figure 7 as the dotted line and the relevant model parameters are listed in Table 2.

Although they both use an optically thick, free-fall density shell in the IR, this model differs quantitatively from the model presented in Stecklum et al. (2002). The central star is of later O-type and cooler surface temperature. The inner dust shell radius is nearly four times smaller and the outer radius nearly twice as compact as in Stecklum et al. These parameters are necessary in order to explain the mid-IR emission in the range 17–37 μm. This work finds that the total luminosity is slightly lower than previous estimates.

Note this model cannot account for the excess emission at 2.2–5.8 μm. One explanation for this emission is clumpiness in the dust cloud, or a cavity opening, which allows short

[7] Ivezic, Z., Nenkova, M., and Elitzur, M. 1996, University of Kentucky, http://www.pa.uky.edu/m~oshe/dusty/

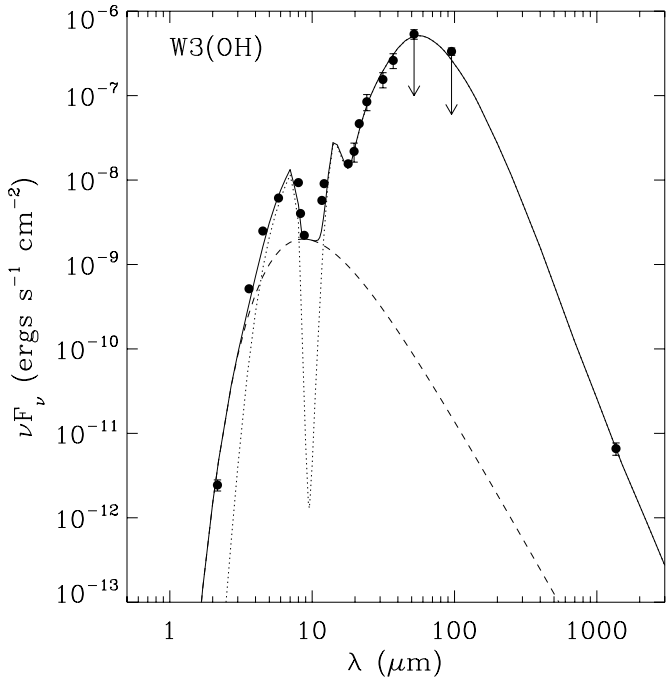

Figure 7. SED of W3(OH) and model fits. Filled circles: combined data points (see the text for references). The *IRAS* fluxes were taken as upper limits, indicated as downward arrows at ∼60 and 100 μm. Dotted line: DUSTY model SED. Dashed line: improvised single-temperature blackbody originating from interior, warm dust emission through a cavity opening. Solid line: total SED from DUSTY model and improvised single-temperature blackbody.

wavelength radiation from warm dust to leak through holes in the cloud. We model radiation from the warmer interior of the shell as a single-temperature (425 K) blackbody component. The plausibility of this model is evident in Figure 7, whereby an excellent fit to the data is achieved with a temperature consistent with that of the interior of the dust shell. There may also be a scattered light component at these wavelengths, but we do not model such a component since its geometry is relatively unconstrained.

An alternative explanation for the excess at 2.2–5.8 μm is a relatively high abundance of very small grains compared with large grains. In order to fit the data at 2.2–5.8 μm, we would need to consider a model with a modified MRN grain size distribution ($q = 4.7$). However, in the ionized region, small grains can become super-heated and destroyed. The emission would come from a relatively high abundance of small grains in the infalling shell; such grains would need to be primordial. Given the jets that are seen in molecular emission, it is most likely that the excess short wavelength radiation originates in a cavity opening. The prediction one can make from this explanation is the presence of continuum emission in the amorphous silicate absorption band at 9.7 μm, which decreases the depth of the absorption feature. Mid-IR spectroscopy in the 8–13 μm window could be used to test this prediction.

4.2. W3(H_2O)

In the radio continuum, the hot core W3(H_2O) consists of three clumps designated as A, B, and C (Wyrowski et al. 1999; Wilner et al. 1999). An early claim to a detection of W3(H_2O) in the infrared came from Keto et al. (1992) who presented ground-based observations at 12.2 μm showing emission at the location of W3(H_2O) C, which lies approximately 4″ east of W3(OH). No emission was seen from sources A and B,

Table 2
DUSTY Parameters for Best-fit Model of the W3(OH) Dust Component

Parameter	Value
T_*	31145 K
R_{in}	576 AU
R_{out}	29942 AU
T_{in}	400 K
T_{out}	26 K
Composition fraction, silicates	53%
Composition fraction, graphite	47%
p	1.5
q	3.5
τ_{37}	2.8

Notes. The parameters are stellar temperature T_*, inner shell radius R_{in}, outer shell radius R_{out}, inner shell boundary temperature T_{in}, outer shell boundary temperature T_{out}, grain composition, density distribution parameter p, grain size distribution parameter q, and optical depth τ_{37} at 37 μm.

which lie approximately 6″ east of W3(OH). However, this observation was not substantiated by Stecklum et al. (2002) who did not detect any emission from these sources at 8–12 μm, despite their spatially resolving W3(OH). In the FORCAST data, the separation of the peaks in the double-peaked line profile (Figure 6) yields the separation between W3(H_2O) and W3(OH), which we find to be 5.″0 at 37.1 μm and 4.″4 at 31.4 μm. Components A and C form a massive protobinary system (Minh & Chen 2007). Based on the gas chemistry of these sources, Minh & Chen (2007) suggest that component A may be more deeply embedded and younger than component C within $<10^4$ yr. This would be consistent with our results that show a wavelength dependence for the 19.7–37.1 μm emission. However, it should be noted that this dependence on wavelength may also result from combined temperature and optical depth gradients.

4.3. Protostars and Young Stars with Disks in the SOFIA Field

We construct SEDs for the four point sources in the FORCAST field and compare them with model SEDs of protostellar and young stellar objects using the online SED fitting tool of Robitaille et al. (2006, 2007). The SEDs and those of the best-fit models are shown in Figure 8. We provide comments on each object in Sections 4.3.1–4.3.4.

4.3.1. 2MASS J02270352+6152357

The best-fitting model for J02270352+6152357 corresponds to a protostellar object with a mass of 3.96 $M_\odot$ and a luminosity of 236 $L_\odot$. The model indicates that this object is young and cool, with an age of just under 5000 yr and a temperature in the low 4000 s of K. It is undergoing active envelope accretion from a massive envelope (11.7 $M_\odot$) onto a low-mass disk (3.92×10^{-3}). The self-consistency of the top ten models with this best-fitting model suggest that this object is indeed a young, intermediate-luminosity protostar.

4.3.2. 2MASS J02270743+6152281

The SED fitting tool produced two families of best-fit models for J02270743+6152281, with the first family headed by the best-fitting SED and the second by the second-best fit. The families differ in the object's stage of envelope accretion and disk formation, with one family representing an object

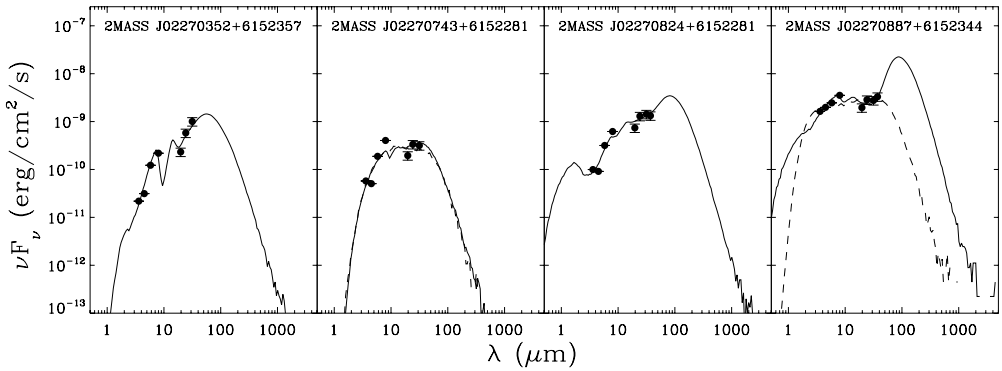

Figure 8. SEDs of the four point sources in the *SOFIA* field (filled circles) and the best-fit protostellar SED model (solid line) from the online SED fitting tool of Robitaille et al. (2006, 2007). For 2MASS J02270743+6152281 and 2MASS J02270887+6152344, the best-fitting alternative, disk-dominated model SEDs are also shown (dashed lines).

still actively undergoing envelope accretion and the other corresponding to a more highly developed disk with a depleted envelope.

The best-fitting (total $\chi^2 = 82.14$) model, representing the first family of models within the top 10 best fits, indicates that this object is a protostellar object with a mass of 5.69 $M_\odot$ and a luminosity of 768 $L_\odot$, surrounded by a relatively substantial envelope (0.153 $M_\odot$) and a smaller disk (3.36×10^{-2} $M_\odot$). This model has a low but nonzero rate of envelope accretion, and suggests an age of 6.47×10^5 yr, with an internal temperature of 16,500 K. These parameters point to an intermediate-luminosity protostar nearing the end of its envelope accretion phase.

The second-best fit (total $\chi^2 = 82.72$), and correspondingly the second family of fits, represents an object with a fully formed disk and a completely depleted envelope no longer accreting material onto the disk. This model protostar has an intermediate mass somewhat higher than the alternative family, of 9.17 $M_\odot$. Its envelope is negligible (10^{-5} $M_\odot$), and its disk has a mass of 2.1×10^{-2} $M_\odot$. It suggests an age of just over 10^6 yr and a temperature of 24,500 K. Given the protostellar mass and these parameters, this family of models likely corresponds to a young star with a circumstellar disk.

The two families of models differ primarily in the presence or absence of an amorphous silicate absorption feature at 9.7 μm, which is typically seen in an envelope-dominated SED. Highly sensitive mid-infrared spectroscopy could be used to resolve the degeneracy between these two families of models.

4.3.3. 2MASS J02270824+6152281

Model fitting for J02270824+6152281 presents a convergent set of parameters. The best-fit model corresponds to a 6.11 $M_\odot$ protostar with a luminosity of 432 $L_\odot$. This model suggests the object is a young protostar (approximately 8000 yr) with a temperature of around 4000 K. The object is embedded in a large 35.1 $M_\odot$ envelope with a disk of mass 1.48×10^{-2} $M_\odot$, indicating that this object is likely experiencing ongoing disk formation. The relatively high envelope accretion rate displayed by this model (1.39×10^{-3} $M_\odot$ yr^{-1}) supports this conclusion. The models predict substantial far-IR emission arising from the envelope, meaning follow-up observations in the far-IR range could confirm our assessment.

4.3.4. 2MASS J02270887+6152344

For J02270887+6152344, the data again result in two possible families of models, representing either an intermediate- to high-mass protostellar object with a large envelope or an older intermediate-mass young star with a clearly defined disk and minimal envelope. The top three fits all corresponded to the former of these models, indicating its greater likelihood for accuracy.

The best-fitting (total $\chi^2 = 15.03$) model for this source represents a 10.5 $M_\odot$ protostar surrounded by a natal dust envelope containing 240 $M_\odot$ of material and a negligible disk. The model object has a luminosity of 3000 $L_\odot$. An age of approximately 2000 yr and a temperature in the 4000s of Kelvins indicate that the object is protostellar in nature.

The second group of well-fitting models is represented by the fourth-best-fitting (total $\chi^2 = 34.34$) model. This model corresponds to a young star of mass 9.8 $M_\odot$, with a depleted envelope (mass approximately 2×10^{-5} $M_\odot$, indicating that the envelope has nearly entirely accreted onto the disk). This model possesses an age of over 10^6 yr and an internal temperature of 25,400 K, indicating a more advanced stage in development than the first family of models presented.

These families of models diverge at far-infrared wavelengths. With only present data, we therefore cannot rule out either the higher-mass, younger protostellar object or the intermediate-mass, more evolved young star. Further observations of this object at far-IR and/or submillimeter wavelengths are required to resolve the degeneracy in the model parameters.

5. CONCLUSIONS

We present *SOFIA*/FORCAST and *Spitzer*/IRAC observations of the UCH II region W3(OH) in the wavelength range 3.6–37.1 μm. These data, combined with other published data, have been used to constrain the optical depth, grain size distribution, and temperature gradient in the dusty shell surrounding the H II region. The total luminosity of W3(OH) is 7.1×10^4 $L_\odot$, indicating that the central star is an O9 star with surface temperature ~31,000 K. A clumpy dust distribution or cavity opening revealing warm interior grains is necessary to explain excess emission at 2.2–4.5 μm.

We detect the hot core W3(H_2O) at 31.4 and 37.1 μm, and constrain its flux density at 19.7–37.1 μm using deconvolved FORCAST images.

In addition, SEDs have been constructed for four young stellar or protostellar objects which lie in the *SOFIA*/FORCAST field. The model SED fitting tool of Robitaille et al. (2006) was used to determine the nature of these objects. 2MASS J02270352+6152357 is an intermediate-luminosity protostar undergoing envelope accretion; 2MASS J02270824+6152281 is most likely a very young intermediate-mass protostar with a

large natal envelope; 2MASS J02270887+6152344 is a high-luminosity object which is either a protostar with ongoing envelope accretion onto a young disk or a young star with a circumstellar disk and a depleted envelope; and 2MASS J02270743+6152281 could be an intermediate-luminosity protostar or potentially a young star with a developed disk and an almost entirely depleted envelope. Further observations in the mid-IR, far-IR, and/or submillimeter range(s) are required to definitively characterize 2MASS J02270887+6152344 and 2MASS J02270743+6152281.

We thank R. Grashius, S. Adams, H. Jakob, A. Reinacher, and U. Lampeter for their *SOFIA* telescope engineering and operations support. We also thank the *SOFIA* flight crews and mission operations team (A. Meyer, N. McKown, C. Kaminski) for their *SOFIA* flight planning and flight support. We are grateful to an anonymous referee for his or her comments which have improved this manuscript. This work is based on observations made with the NASA/DLR *Stratospheric Observatory for Infrared Astronomy* (*SOFIA*). *SOFIA* science mission operations are conducted jointly by the Universities Space Research Association, Inc. (USRA), under NASA contract NAS2-97001, and the Deutsches SOFIA Institut (DSI) under DLR contract 50 OK 0901. Financial support for FORCAST was provided to Cornell by NASA through award 8500-98-014 issued by USRA. This work is based in part on observations made with the *Spitzer Space Telescope*, which is operated by the Jet Propulsion Laboratory, California Institute of Technology under a contract with NASA. This publication makes use of data products from the Two Micron All Sky Survey, which is a joint project of the University of Massachusetts and the Infrared Processing and Analysis Center, funded by the National Aeronautics and Space Administration and the National Science Foundation. This research has made use of the NASA/IPAC Infrared Science ArChive, which is operated by the Jet Propulsion Laboratory, California Institute of Technology, under contract with the National Aeronautics and Space Administration. This research has made use of NASA's Astrophysics Data System Abstract Service.

Facilities: Spitzer, *SOFIA*, *IRAS*

REFERENCES

Adams, J. D., Herter, T. L., Gull, G. E., et al. 2010, Proc. SPIE, 7735, 62
Campbell, M. F., Lester, D. F., Harvey, P. M., & Joy, M. 1989, ApJ, 345, 298
Chini, R., Krügel, E., & Kreysa, E. 1986, A&A, 167, 315
Churchwell, E. 2002, ARA&A, 40, 27
Conti, P., Rho, J., Furness, J., & Crowther, P. A. 2008, in Proc. IAU 250, Non-Stable Stars, ed. F. Bresolin, P. A. Crowther, & J. Puls (Cambridge: Cambridge Univ. Press), 285
Draine, B. T., & Lee, H. M. 1984, ApJ, 285, 89
Egan, M. P., Price, S. D., Moshir, M. M., et al. 1999, Air Force Laboratory Technical Report No. AFRL-VS-TR-1999-1522
Fazio, G. G., Hora, J. L., Allen, L. E., et al. 2004, ApJS, 154, 10
HaChisuka, K., Brunthaler, A., Menten, K. M., et al. 2006, ApJ, 645, 337
Hartmann, L. 2009, Accretion Processes in Astrophsics (2nd ed,; Cambridge: Cambridge Univ. Press)
Herter, T. L., Adams, J. D., De Buizer, J. M., et al. 2012, ApJ, 749, L18
Hora, J. L., Fazio, G. G., Allen, L. E., et al. 2004, Proc. SPIE, 5487, 77
Keto, E., Proctor, D., Ball, R., Arens, J., & Jernigan, G. 1992, ApJ, 401, L113
Lucy, L. B. 1974, AJ, 79, 745
Mader, G. L., Johnston, K. J., & Moran, J. M. 1978, ApJ, 224, 115
Makovoz, D., & Khan, I. 2005, in ASP Conf. Ser. 347, Astronomical Data Analysis Software and Systems VI, ed. P. L. Shopbell, M. C. Britton, & R. Ebert (San Francisco, CA: ASP), 81
Mathis, J. S., Rumpl, W., & Nordsieck, K. H. 1977, ApJ, 217, 425
Megeath, S. T., Townsley, L. K., Oey, M. S., & Tieftrunk, A. R. 2008, in Handbook of Star Forming Regions, Volume I: The Northern Sky ASP Monograph Publications, ed. B. Reipurth, Vol. 4 (San Francisco, CA: ASP), 264
Menten, K. M., Reid, M. J., Pratap, P., Moran, J. M., & Wilson, T. L. 1992, ApJ, 401, L39
Minh, Y. C., & Chen, H.-R. 2007, in IAU Sump. 237, Triggered Star Formation in a Turbulent Interstellar Medium, ed. B. G. Elmegreen & J. Palous (Cambridge: Cambridge Univ. Press), 448
Moore, T. J. T., Bretherton, D. E., Fujiyoshi, T., et al. 2007, MNRAS, 379, 663
Richardson, W. H. 1972, J. Opt. Soc. Am., 62, 55
Robitaille, T. P., Whitney, B. A., Indebetouw, R., & Wood, K. 2007, ApJS, 169, 328
Robitaille, T. P., Whitney, B. A., Indebetouw, R., Wood, K., & Denzmore, P. 2006, ApJS, 167, 256
Ruch, G., Jones, T., Woodward, C., Polomski, E., & Gehrz, R. 2007, ApJ, 654, 338
Schuster, M., Marengo, M., & Patten, B. 2006, Proc. SPIE, 6270, 65
Sellgren, K. 1984, ApJ, 277, 623
Skrutskie, M. F., Cutri, R. M., Stiening, R., et al. 2006, AJ, 131, 1163
Stecklum, B., Brandl, B., Henning, T., et al. 2002, A&A, 392, 1025
Tieftrunk, A. R., Megeath, S. T., Wilson, T. L., & Rayner, J. T. 1998, A&A, 336, 991
Turner, J. L., & Welch, W. J. 1984, ApJ, 287, L81
Werner, M. W., Roellig, T. L., Low, F. J., et al. 2004, ApJS, 154, 1
Wilner, D. J., Reid, M. J., & Menten, K. M. 1999, ApJ, 513, 775
Wilson, T. L., Bieging, J., & Downes, D. 1978, A&A, 63, 1
Wink, J. E., Duvert, G., Guilloteau, S., et al. 1994, A&A, 281, 505
Wynn-Williams, C. G., Becklin, E. E., & Neugebauer, G. 1972, MNRAS, 160, 1
Wyrowski, F., Hofner, P., SChilke, P., et al. 1997, A&A, 320, L17
Wyrowski, F., SChilke, P., Walmsley, C. M., & Menten, K. M. 1999, ApJ, 514, L43
Young, E. T., Becklin, E. E., De Buizer, J. M., et al. 2012, ApJ, 749L, 17
Zeng, Q., Hermsen, W., Wilson, T. L., & Batria, W. 1984, A&A, 140, 169